RESEARCH ARTICLE OPEN ACCESS

Learning-Based Rapid Phase-Aberration Correction and Control for Robot-Assisted MRI-Guided Low-/High-Intensity Focused Ultrasound Treatments

Jing Dai[1,2,3] (iD) | Xiaomei Wang[1] | Bohao Zhu[1] | Liyuan Liang[2,4] | Hing-Chiu Chang[2,4] | James Lam[1] | Xiaochen Xie[5,6] | Ka-Wai Kwok[1,2,3] (iD)

[1]Department of Mechanical Engineering, The University of Hong Kong, Hong Kong, People's Republic of China | [2]Multi-Scale Medical Robotics Center Ltd., Hong Kong, People's Republic of China | [3]Department of Mechanical and Automation Engineering, The Chinese University of Hong Kong, Hong Kong, People's Republic of China | [4]Department of Biomedical Engineering, The Chinese University of Hong Kong, Hong Kong, People's Republic of China | [5]School of Intelligence Science and Engineering, Harbin Institute of Technology, Shenzhen, People's Republic of China | [6]Institute for Automatic Control and Complex Systems, University of Duisburg-Essen, Duisburg, Germany

Correspondence: Xiaochen Xie (xiexiaochen@hit.edu.cn) | Ka-Wai Kwok (kwokkw@mae.cuhk.edu.hk)

ABSTRACT

Magnetic resonance imaging (MRI)-guided focused ultrasound (MRg-FUS) is an effective and noninvasive procedure for treating diseases such as neurological disorders. Phase adjustment on ultrasound transducers can only achieve a limited focal-spot steering range. When treating large abdominopelvic targets, mechanical adjustment on the transducers' position and orientation is the prerequisite for enlarging the steering range. Therefore, we previously designed an MRI-guided robot to manipulate the transducers to offer sufficient focal-spot movement range. This could provide more modulation solutions to constructive ultrasound interference. However, full-wave ultrasound propagation inside a patient's heterogeneous abdominal media is complex and nonlinear, posing significant challenges in ultrasound modulation and beam motion control. Here, we propose a novel learning-based phase-aberration correction and model-free control framework for robot-assisted MRg-FUS treatments. The correction policy guarantees rapid aberration compensation within 5.0 ms. Submillimeter refocusing accuracy is achieved in both the liver (0.32 mm) and pancreas (0.51 mm), meeting clinical requirements for focal targeting. Our controller can accommodate nonlinear phase actuation with fast convergence (< 5.7 ms) and ensure accurate positional tracking with a mean error of 0.26 mm, without prior knowledge of inhomogeneous media. Compared with the conventional model-based method, it contributes to 61.77%–70.39% mean error reduction without requiring model parameter tuning.

1 | Introduction

Focused ultrasound (FUS) (Kosnoff et al. 2024) is a safe and effective therapeutic technology, with the unique advantage of being totally noninvasive in nature (Wu et al. 2024). Magnetic resonance imaging (MRI) has been introduced to guide FUS procedures due to its ability to monitor tissue temperature in real-time through MR thermometry (Dillon et al. 2018) (Figure 1a) and
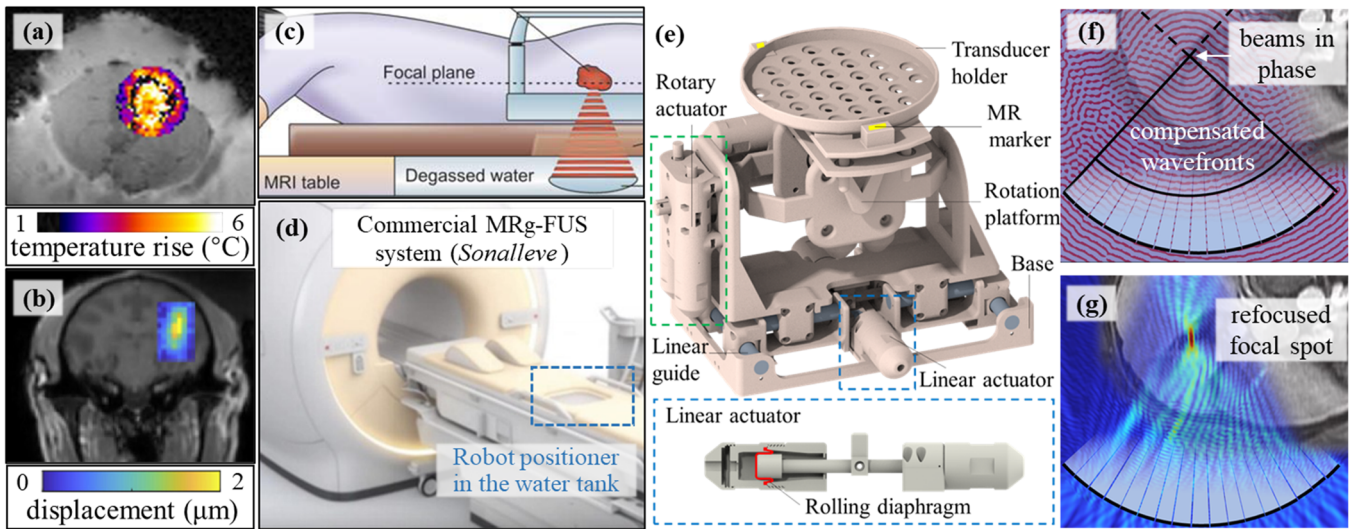

FIGURE 1 | (a) Thermal map measured by magnetic resonance (MR) thermometry during the high-intensity FUS (HIFU) process in a mimicking model (Image source: Guillemin et al. 2019). (b) Micron-scale tissue displacement map detected by MR acoustic radiation force imaging (MR-ARFI) in a macaque brain (Image source: Luo et al. 2022). (c) Schematic of magnetic resonance imaging (MRI)-guided focused ultrasound (MRg-FUS) for abdominopelvic organ diseases, with the transducer placed inside a water tank (Image source: Ljubic et al. 2009). (d) Example of a commercial robotic MRg-FUS platform, that is, *Sonalleve* (Image source: Wong et al. 2021). (e) MRI-guided robotic platform for abdominopelvic FUS treatment. Rolling diaphragm-sealed linear actuators can eliminate sliding friction, allowing for smooth movement of the platform. (f) Phase field distribution after phase-aberration correction. Ultrasound wavefronts are compensated and the beams are in phase at the target point. (g) Pressure field distribution after aberration correction. Beams are refocused at the predefined target point. [Color figure can be viewed at wileyonlinelibrary.com]

visualize ultrasound beams (Figure 1b) via MR acoustic radiation force imaging (MR-ARFI) (Vyas et al. 2014). With these advances in MRI (Fang et al. 2022), MRI-guided FUS (MRg-FUS) (Meng et al. 2022) has emerged as a promising modality with considerable clinical potential in a variety of applications (Sun et al. 2017), for example, ablation (Hynynen 2020; Rouvière et al. 2012), blood–brain barrier opening (Lipsman et al. 2018; McMahon et al. 2021), and neuromodulation (Hou et al. 2021; Meng et al. 2021).

To steer the FUS focal spot, it is common practice to *electronically* modulate the phases of a *fixed* transducer array; however, this typically has a limited focal-spot steering range (<Ø3.5 cm) (Figure 1c). When treating large abdominopelvic organs that involve big/multiple targets, additional mechanical displacement of the transducers is required to provide sufficient movement of the focal spot. MRI-guided robots, such as *Sonalleve* platform (Figure 1d), have emerged as a solution to mechanically adjust the transducer's position and orientation, substantially enlarging the focal-spot movement range. Besides, such robotic transducer manipulation would eliminate the need to transfer patients in and out of the MRI scanner bore for manual transducer calibration, thus reducing the procedure time. A few MRg-FUS robotic systems that are currently available in the market have been approved by the U.S. Food and Drug Administration (FDA) (Hyvärinen et al. 2022; Santos et al. 2020); however, they are primarily targeted towards shallow and weakly heterogeneous *pelvic* anatomy. In contrast, abdominal tissues are highly heterogeneous, with variations in tissue structure (e.g., thickness) and acoustic properties (e.g., sound speed) that result in *phase aberration*, that is, relative phase shifts varying along the FUS wavefront (Martin et al. 2024). This heterogeneity results in substantial focal distortion, and focal shift on a non-negligible scale, especially for

deep-seated targets. (Kyriakou et al. 2015). High-intensity FUS (HIFU) safety issue is another concern. Even in the case of optimal modulation to compensate for phase aberration, excessive ultrasound exposure to a particular skin area may cause skin burn.

Therefore, we previously designed a 5 degree of freedom (DoF) MRI-guided robotic platform (Figure 1e) (Dai et al. 2021), which was the first-of-its-kind robot system to handle the challenges faced in abdominopelvic FUS. Robotic transducer manipulation could provide large-range foci movement with more modulation solutions to accomplish constructive ultrasound interference. Combined with a remote center of motion mechanism, the same target points could remain in focus while dispersing heat accumulation across a larger/varying skin area, preventing skin burn. Rolling diaphragm-based linear actuators were also designed to ensure accurate manipulation (0.2 mm in translation, 0.4° in rotation) of the transducer holder.

To generate constructive ultrasound interference, phase modulation (Shen et al. 2024a) for aberration compensation (Figure 1f,g) has to be coordinated with robotic transducer positioning. To date, several aberration correction techniques have been proposed for beam refocusing (Rosnitskiy et al. 2024), some of which compensate for the aberrations by observing ultrasound interference using MRI (Su et al. 2022). As a gold standard, the hydrophone-based method can perform excellent correction by measuring phases using an implantable hydrophone. However, its invasive nature makes it impractical in clinical usage (Almquist et al. 2016). Instead, full-wave simulation-based methods can provide safe and precise phase-aberration correction (Kaye et al. 2012), for example, using the finite-difference time-domain (FDTD) approach

(Kyriakou et al. 2015). However, simulation-based methods can be time-consuming (hour level) and demand significant computational resources, which is usually not feasible in clinical practice (Almquist et al. 2016). To speed up phase correction, analytical approaches have been proposed, for example, the angular spectrum approach (Schoen et al. 2019). The ultrasound wave is intuitively assumed to travel along a straight line in heterogeneous tissues, with physical effects (e.g., reflection, refraction) not taken into account. This would reduce full-wave model complexity to enable computationally efficient correction within minutes. However, in practice, beam interference in the human abdomen could not avoid the nature of complex physical effects. Simplified analytical modeling would result in a loss of accuracy, as there exists a trade-off between correction accuracy and computational time/model complexity (Almquist et al. 2016). The MR-ARFI-based method (Mougenot et al. 2012) can derive the optimal phase analytically or iteratively. For a single target, element-to-element ARFI measurements are necessary to compensate for aberration. However, in practice, a large region of interest (ROI) consists of hundreds of target points. Correcting the targeting for all target points requires repeated measurements, substantially prolonging the procedure time (Kaye et al. 2012). Therefore, the previous correction methods heavily rely on computationally demanding algorithms, suffer from inaccurate analytical modeling, or require extensive time-consuming MR-ARFI measurements. Rapid ultrasound transduction enabling accurate *full-wave* correction remains a significant challenge (Kyriakou et al. 2015), particularly for the treatment of abdominopelvic organ diseases. This may greatly limit the clinical adoption of transabdominal MRg-FUS on a large scale.

Apart from beam refocusing for point-by-point targeting, beam motion control is also crucial in some FUS applications (e.g., regional hyperthermia, Partanen et al. 2012), which enables the focal spot to *continuously* track within a target *region*. Inverse mapping from the beam motion to actuation input (i.e., phase pattern) has to be modeled to enable this. Several model-based open-loop approaches have been proposed for continuous tracking. The mapping models are often simplified to avoid modeling the complex, nonlinear full-wave propagation through heterogeneous tissues. Therefore, the homogeneous medium assumption was popularly proposed; however, such an overly ideal assumption and oversimplification would lead to substantial degradation in model reliability in practice. Other methods based on ray-tracing theory have also been investigated for real-time control, but such simple geometric solutions (Kyriakou et al. 2014) would still inevitably reduce the tracking accuracy. The aforementioned methods are likely limited to scenarios with weak tissue heterogeneity (e.g., in rat models), which are far from adoption in human abdominal treatments (Gerhardson et al. 2017). Moreover, searching for acoustic parameters poses a further challenge in motion mapping modeling and convergence of the model-based controller, as organ tissues are inherently spatially heterogeneous with complex structures (e.g., fat, fascia, veins) (Johnson et al. 2016).

Considering the challenges in modeling complexity and uncertainty, model-free control approaches have been proposed to enhance real-time and precise beam motion control, with the potential to outperform analytical approaches (Lee et al. 2017).

Recently, machine learning (ML) techniques have showcased their effectiveness in model-free control (X. Wang et al. 2023) by accommodating modeling uncertainties in a *closed-loop* manner using sensory data, without having to construct an analytical model. For example, nonparametric ML algorithms (Lee et al. 2017) have been introduced to directly generate an inverse mapping for soft robot control (Fang et al. 2021; Kwok et al. 2022). Besides the modeling complexity challenges, the existing model-based beam steering strategies would also suffer from a lack of *positional* feedback. Although MR thermometry guidance has been investigated, it can only provide thermal maps of the targeted tissue, instead of the focal spot position. This pitfall becomes apparent in low-intensity FUS (LIFU) applications (Hou et al. 2024; F. Li, Gallego, et al. 2024), which do not generate appreciable thermal effects in tissues. Therefore, the combination of ML techniques (Ng et al. 2021) and model-free control with sensing feedback has significant potential advantages, especially in the context of MRg-FUS treatments.

Currently, very few methods could ensure rapid and accurate phase-aberration correction for MRg-FUS treatments. Besides, *closed-loop* model-free control of MRg-FUS systems has yet to be explored for simultaneous ultrasound beam focusing and steering. Therefore, our motivation is to utilize ML-based algorithms to offer efficient and accurate solutions to full-wave ultrasound modulation. Learning-based approaches could accommodate nonlinear phase actuation for beam motion control. Additionally, effective image feedback capable of providing focal-spot position information is expected to be incorporated to close the control loop for constructive beam interference. To this end, we propose a novel learning-based correction and *closed-loop* model-free control framework for robot-assisted transabdominal MRg-FUS treatments. Two inverse mappings from task space to actuation space are directly approximated by an extreme learning machine (ELM) (J. Wang et al. 2022) model, without prior knowledge of inhomogeneous media. Notably, most previous studies only concentrated on aberration correction for single-point refocusing, whereas our approach aims to explore both correction and control functions for a broader range of applications. Our key contributions are listed as follows:

1. Development of a learning-based full-wave solver to *rapidly* (< 5.0 ms) correct phase-aberration, thus allowing *precise* focal targeting (liver: 0.32 mm; pancreas: 0.51 mm), without prior knowledge of heterogeneous media.

2. The *first* attempt to propose an ELM-based controller to enable robust *simultaneous* beam refocusing and steering (0.26 mm), such that inverse mapping of a redundantly actuated phased-array system can be directly approximated in real time (< 5.7 ms), without complicated modeling of acoustic wave propagation. Image feedback is incorporated to provide focal position information, allowing constructive acoustic beam interference in a closed-loop manner.

3. Proof-of-concept *validation* of the correction and control policies using MR images, to make effective use of robotic manipulation for MRg-FUS treatments, such as enlarging the movement range of focal spot and reducing the risk of skin burn.

2 | Related Work

Ultrasound transduction planning for MRg-FUS treatments is challenging within the highly heterogenous abdomen, due to the nonlinear propagation of full-wave ultrasound. To ensure constructive ultrasound interference, extensive effort has been devoted to developing phase aberration correction methods. These can be categorized into two major groups: (1) signal-based and (2) model-based approaches. An intuitive solution is to apply low frequency (e.g., < 200 kHz) for ultrasound beam focusing, as lower-frequency ultrasound is less susceptible to phase aberrations in heterogenous tissues, as compared with ultrasound with higher frequency (Yeats and Hall 2023). However, high-frequency ultrasound waves (e.g., > 500 kHz) are desirable because they can generate small focal spots for precise treatment.

Signal-based methods generally determine phase errors by measuring ultrasound signals from the focus directly. Hynynen et al. positioned an "implanted" hydrophone at the target location of an Ex Vivo skull (Kyriakou et al. 2014). Each transducer element was powered individually to measure the phase shifts. The inverted phases were then applied to the elements, resulting in precise beam focusing. Such a hydrophone-based approach has become a "gold standard" in experimental studies; however, the inherently invasive method is impractical in-vivo. Therefore, several studies have attempted to investigate phase-correction approaches in a noninvasive manner. Macoskey et al. reported that acoustic cavitation emission shockwaves can be detected by transducer arrays, thus determining element-to-element phase differences for aberration correction in histotripsy application (Macoskey et al. 2018). They employed a 500-kHz phased-array transducer to transmit and receive ultrasound waves, so as to recover the ultrasound pressure at the target region. Other paradigms have been also proposed to resolve the phase aberration problem. The MR-ARFI-based method is a typical means to correct the phase aberrations. Vyas et al. introduced a hybrid MR-ARFI approach, which uses an MR-ARFI image in combination with ultrasound simulations to estimate the corrected phases (Vyas et al. 2014).

Apart from signal-based methods, model-based methods have also been investigated, with the aim to compute phases by modeling acoustic propagation using medical images. Kyriakou et al. utilized a FDTD acoustic solver to perform full-wave modulations (Kyriakou et al. 2015). MR images were segmented to develop an anatomical head model for numerical simulations. Almquist et al. developed a full-wave simulation-based method for phase aberration correction in HIFU treatments (Almquist et al. 2016). Corrections were tested on an Ex Vivo human skull flap, achieving an eight-fold improvement in computational time over the FDTD-based simulation method (Marquet et al. 2009). These full-wave model-based methods could ensure accurate focal targeting, but high computational costs associated with extensive simulation time usually limit them in clinical practice. Many studies have attempted to investigate analytical-based approaches for *efficient* phase correction. Jin et al. explored the feasibility of ray-based modeling for phase correction (Jin et al. 2020), capable of computing the phases around 402.1 ms for each target point. The angular spectrum approach (Schoen et al. 2021) developed by Schoen

et al. also enables millisecond-level (166 ± 37 ms) phase modulation (Schoen et al. 2019; Shen et al. 2024b). Such analytical methods based on geometric ray-tracing theory result in improved computational efficiency over the full-wave methods. However, simplified analytical modeling would compromise targeting accuracy, as complex physical effects are not considered in the acoustic propagation process.

3 | Materials and Methods

This section presents the learning-based correction and control framework dedicated to transabdominal MRg-FUS. Details of data collection, model training, and model testing are also presented.

3.1 | Task Space Definition

First, we defined the inverse mapping from actuation space to task space. The phased array system's task space is defined as the beam state. It can be represented as $[\boldsymbol{p}^{\mathrm{T}}, s]^{\mathrm{T}} \in \mathbb{R}^3$, where $\boldsymbol{p} \in \mathbb{R}^2$ and $s \in \mathbb{R}$, respectively, are the focal point position and the focal area. Note that the focal point is denoted by the point with peak acoustic intensity, and the focal area is calculated with the -3 dB intensity reduction of the focal zone. The actuation space is the driving phase of the phased array. It can be represented as $\boldsymbol{\varphi} \in \mathbb{R}^n$, where n is the number of array elements, $n = 18$ in this study. The focal spot motion vector at the time step k is detected by calculating the focal point positions between adjacent intensity maps, which is denoted as $\Delta \boldsymbol{p}(k) = \boldsymbol{p}(k+1) - \boldsymbol{p}(k) \in \mathbb{R}^2$. Second, we proposed the correction policy to realize beam focusing at a particular target point inside the human abdomen.

As shown in Figure 2, the phases can be adjusted individually to compensate for phase aberration of the wavefront. We also developed a control policy to realize simultaneous beam refocusing and steering. The driving phase generated by the controller would allow the focused beam to continuously track along the predefined paths, such that the focal spot can cover the whole target region. The ELM model (J. Wang et al. 2022) is adopted to establish the two inverse mappings, that is, the phase-aberration correction model and the motion mapping model. The ELM model operates as a single hidden layer feedforward neural network (SLFN). The SLFN output weights, which represent connections between the hidden-layer nodes and the output nodes, can be directly computed by the Moore-Penrose inverse, which can be determined in a single run. As a result, the ELM model is advantageous in rapid initialization and model convergence, which does not require gradient-based backpropagation or learning rate tuning.

3.2 | Phase Correction and Closed-Loop Control

The architecture of the proposed correction and control framework is shown in Figure 3. Depending on particular applications, the input unit of the framework can provide two positional commands, either the target points or the reference

trajectories. Since amplitude aberration can be neglected in LIFU (Zhou et al. 2017) owing to negligible temperature increase, the two policies would be feasible in LIFU.

To achieve closed-loop tracking control, an accurate inverse mapping of the redundantly actuated phase-array system must be formed. Owing to phase actuation nonlinearity, precise steering of the focal spot in a large ROI could be challenging. Thus, as shown in Figure 3a, we implemented a learning-based model to establish the motion mapping from the prescribed focal spot movements to phase signal commands. Given the current driving phases of the transducers, and the displacement between the current focus point and target point, our motion mapping model can predict the phase changes for phased-array
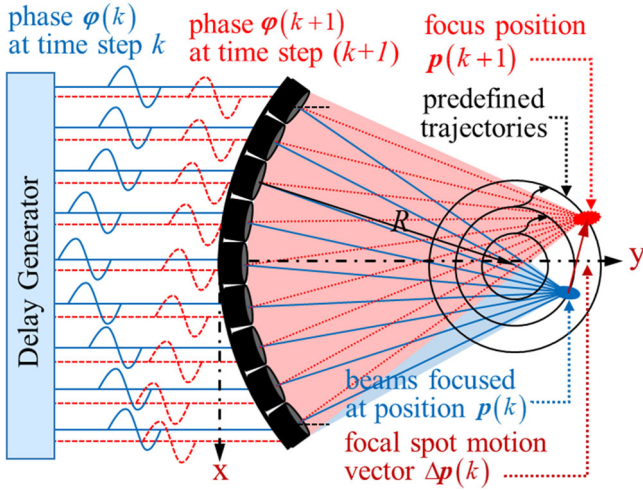

FIGURE 2 | Diagram of ultrasound transduction planning with a phased-array transducer. The beams traversing heterogeneous media can be focused at the predefined targeted point $\boldsymbol{p}$ with corrected phase pattern $\boldsymbol{\varphi}$. These beams can also be simultaneously focused and steered from position $\boldsymbol{p}(k)$ to $\boldsymbol{p}(k+1)$ along the predefined trajectories by adjusting the phase pattern, where k denotes the time step. [Color figure can be viewed at wileyonlinelibrary.com]

actuation. The focal point position detected by the acoustic intensity map acts as sensing feedback to close the control loop. We proposed to use the desired focal spot motion $\Delta\boldsymbol{p}^*(...)$, phase pattern $\boldsymbol{\varphi}(...)$, and phase change $\Delta\boldsymbol{\varphi}(...)$ to directly estimate the inverse motion mapping $K(...)$. Note that the superscript "*" denotes the desired variable in this study. The control objective is to estimate phase change $\Delta\boldsymbol{\varphi}(k)$ with desired focal motion $\Delta\boldsymbol{p}^*(k)$ at time step k.

Training: The pre-training procedure would collect the focal spot position and corresponding phase actuation at each time step. The actuation sequence $\boldsymbol{\Psi} = [\boldsymbol{\varphi}(1)\ \boldsymbol{\varphi}(2)\ ...\ \boldsymbol{\varphi}(N_0)] \in \mathbb{R}^{n \times N0}$ for data exploration is predefined, such that the whole ROI can be "filled" with N_0 target samples. The phase change sequence can be obtained as $\Delta\boldsymbol{\Psi} = [\Delta\boldsymbol{\varphi}(1)\ \Delta\boldsymbol{\varphi}(2)\ ...\ \Delta\boldsymbol{\varphi}(N_0)] \in \mathbb{R}^{n \times N0}$, where the phase change of ith training sample is expressed as $\Delta\boldsymbol{\varphi}(i) = \boldsymbol{\varphi}(i+1) - \boldsymbol{\varphi}(i)$, $i = 1, 2, ..., N_0$. The desired focal spot motion is calculated by $\Delta\boldsymbol{p}^*(i) = \boldsymbol{p}^*(i+1) - \boldsymbol{p}(i)$, where $\boldsymbol{p}^*(...)$ denotes the desired target position. It can be used to form the motion sequence $\Delta\boldsymbol{P}^* = [\Delta\boldsymbol{p}^*(1)\ \Delta\boldsymbol{p}^*(2)\ ...\ \Delta\boldsymbol{p}^*(N_0)] \in \mathbb{R}^{2 \times N0}$. With $[\boldsymbol{\Psi}\ \Delta\boldsymbol{P}^*]^T \in \mathbb{R}^{(n+2) \times N0}$ as the input and $\Delta\boldsymbol{\Psi}$ as the output, we can train the motion mapping $K(...)$ represented as

$$\Delta\boldsymbol{\varphi}(i) = K(\boldsymbol{\varphi}(i), \Delta\boldsymbol{p}^*(i)), i = 1, 2, ..., N_0 \quad (1)$$

The input layer of the motion mapping model consists of $m + n$ neurons, where m and n represent the dimensions of the desired focal spot motion and the phase pattern, respectively. In this study, we set $m = 2$ and $n = 18$. The variable λ denotes the number of the model's hidden neurons, which is set as 1500. Note that this hyperparameter can be tuned to enhance prediction accuracy in particular data sets.

Prediction: Referring to the desired focal spot position and current phase pattern at the time step k, the estimated phase change $\Delta\boldsymbol{\varphi}_w$ can be obtained through the trained motion mapping

$$\Delta\boldsymbol{\varphi}_w(k) = K(\boldsymbol{\varphi}(k), \Delta\boldsymbol{p}^*(k)), k = 1, 2, ... \quad (2)$$
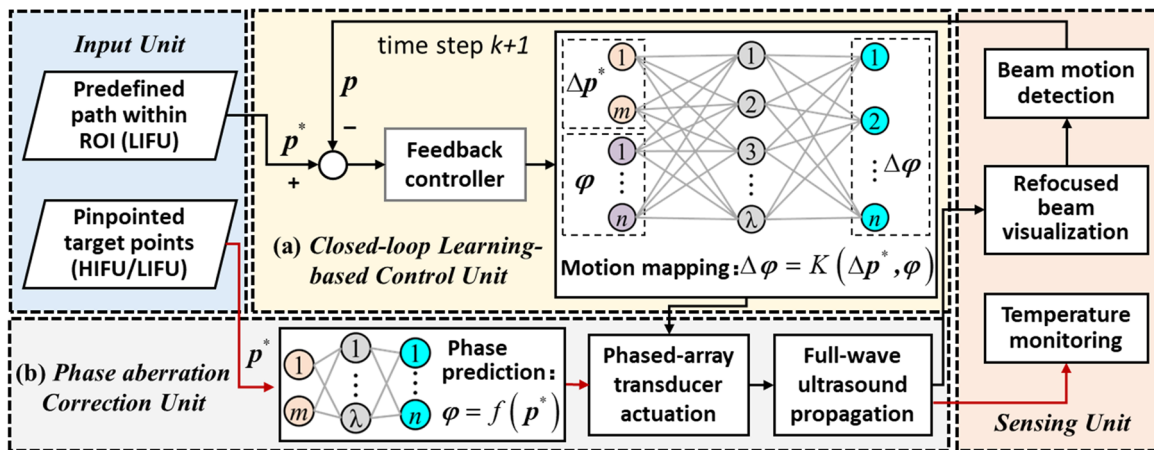

FIGURE 3 | Architecture of the proposed learning-based controller and correction method. (a) Closed-loop control for focal-spot position tracking. The focal position displacement and the phase pattern act as inputs of the extreme learning machine (ELM)-based model, which is mapped to the phase changes of the transducer elements. (b) Phase-aberration correction policy. Mapping from the predefined target position to the associated phase pattern is learned to determine the required phases. The superscript "*" denotes the desired variable. [Color figure can be viewed at wileyonlinelibrary.com]

Regarding the phase-aberration correction model in Figure 3b, to compensate for phase aberration, mapping from the target position p^* to the driving phase φ has to be determined. The focal position can be directly extracted from the intensity map in the sensing unit. N_1 target samples are collected for the correction model training. The actuation sequence of n elements and the target position is $\Psi = [\varphi(1)\ \varphi(2)\ ...\ \varphi(N_1)] \in \mathbb{R}^{n \times N1}$ and $P = [p^*(1)\ p^*(2)\ ...\ p^*(N_0)] \in \mathbb{R}^{2 \times N1}$, respectively. Using the ELM network, with P as the input and Ψ as the output, the phase correction model $f(...)$ can be represented as $\varphi(i) = f(p^*(i))$, $i = 1, 2,..., N_1$. Here, the model's input neuron number is 2, and the output neuron number is 18. Its hidden neuron number was set as 1500, which is the same as the motion mapping model. To perform phase aberration compensation and point-by-point targeting tests, given the kth predefined testing target point $p^*(k)$, the estimated phase pattern φ_w can be directly calculated through the learned model by

$$\varphi_w(k) = f(p^*(k)), \quad k = 1, 2, ... \quad (3)$$

3.3 | Data Collection and Model Implementation Details

A simulator was built to conduct all the experiments, that is, Comsol Multiphysics and Matlab co-simulator (Comsol Inc.). It serves as a validation platform to assess the feasibility of our framework in LIFU/HIFU applications. Before validation of the correction and control policies, data sets should be collected to train the correction and control models. First, high-quality raw MR images should be acquired, so as to reconstruct a three-dimensional (3D) geometric anatomy structure model. Here, an out-phase T1-weighted axial image from a retrospective database (Kavur et al. 2021) was selected. This database was obtained on a 1.5 T Philips MRI scanner from the Department of Radiology, Dokuz Eylul University Hospital, Izmir, Turkey. Key imaging parameters were as follows: TE = 2.3 ms, TR = 116.5 ms, flip angle = 80°, slice thickness = 8.0 mm.

Since a series of two-dimensional (2D)-focused beams with the same target point can be incrementally reconstructed to form the 3D-focused beam, we validated our idea based on a 2D anatomical model for ease of simulations in this proof-of-concept study. As shown in Figure 4a, the color map demonstrates visible

heterogeneous tissue distribution, including property differences (e.g., sound speed) and spatial variations (e.g., tissue thickness). Then, the anatomical regions in the MR slice were identified and delineated, and the anatomical structures (e.g., muscle, fat, skin, bone) were segmented using ITK-SNAP. Targets in the predefined ROI deep inside the organ were selected as training samples (Figure 4b). With the segmented anatomical model, FE modeling was conducted for raw data collection in the co-simulator, including geometry definition, material property assignment, and meshing.

With the MRI-based anatomical model, the data set can be collected for model training (Figure 4c). An acoustic window under the abdomen was determined for constructive ultrasound interference, where a transducer with 18 elements (Ø7 mm) is 10 cm beneath the skin surface. Note that transducer settings, such as element diameter and element placement, can be further tuned depending on particular applications. In general, the transducer manufacturers could offer customized solutions to the transducer plates/elements in terms of size, shape, and functionality (e.g. frequency), thus comprising a phased-array transducer for effective HIFU/LIFU applications. The examples include Siansonic (Ø > 4 mm, frequency > 400 kHz) (Siansonic 2023) and CTS Corporation (length > 0.4 mm, width > 1.5 mm, frequency > 500 kHz) (CTS 2024). As using a low operating frequency (e.g., 220 kHz) would lead to severe reflections, undesired standing waves, and unpredictable hotspots within the abdominal cavity, a higher frequency should be applied. Considering a wide range of applications, a medium frequency, 550 kHz, was set as a representative throughout the simulations. The time-reversal method (Kyriakou et al. 2014), as a gold standard, was used for transduction planning that enables all the individual beams to be in phase at the target point. For each training sample, a point element is allocated at the target, transmitting ultrasound waves in all directions. With such backward wave propagation, the elements acting as receivers will record the corresponding time-of-flight (ToF) in the time domain. As a result, the raw data pairs (i.e., ToF and target position) can be recorded locally, where the outlier data pairs were removed to maintain the data set quality. Subsequently, phase patterns can be computed using ToFs to obtain ground-truth phase-position pairs for model training and validation.

To prepare the data sets for the correction and control policies, a total of 649 target points in the liver ROI were selected. The
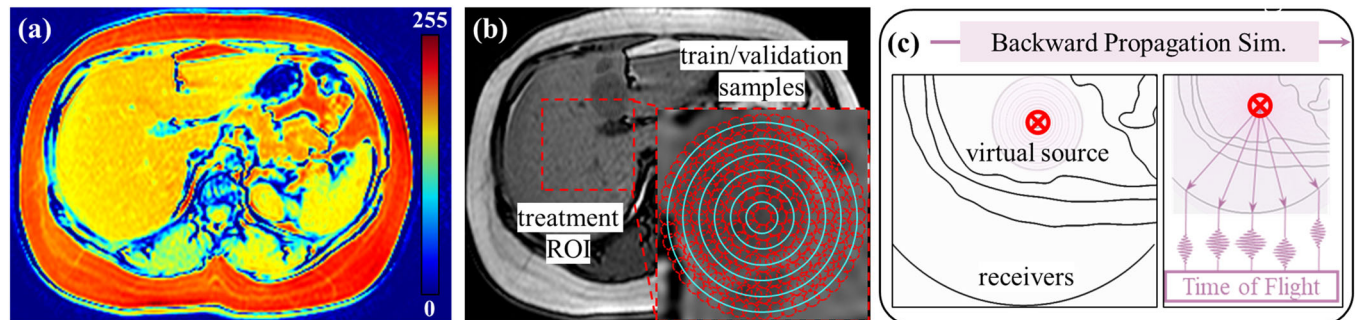

FIGURE 4 | (a) Jet color map representing the intensity of image pixels, showing severe tissue heterogeneity. (b) Samples collected for model training and validation (source from: Kavur et al. 2021). The samples are distributed in concentric circles (solid green) and are depicted using red circles. (c) Flow of phase-position data pair acquisition. Using the time-reversal method, the time-of-flight of each transducer element can be collected after acoustic backward propagation. [Color figure can be viewed at wileyonlinelibrary.com]

data pairs (i.e., ToF and target position) at each target were collected. We then obtain the first data set, which includes 619 training samples for correction model training and 30 validation samples for phase aberration analysis. We also selected 77 testing samples to evaluate the focal targeting performance. Provided with the raw data pairs, at each target point, corresponding focal spot motion $\Delta p^*(...)$, phase pattern $\varphi(...)$, and phase change $\Delta\varphi(...)$ can be obtained, thus producing 5500 samples for motion mapping training. To evaluate the focal targeting performance in the pancreas, a data set was also collected, comprising 57 training samples and 9 testing samples.

With the trained models using the corresponding data sets, the predicted phases were applied for experimental validation. Acoustic simulations on forward wave propagation in the frequency domain were performed to evaluate the targeting accuracy. An AI-corrected (AI-C) condition indicates the phases computed by our model. A non-corrected (NC) case means the phase is calculated using geometry-based equations ignoring phase aberration (Dillon et al. 2018). The targeting accuracy improvement of the AI-C case over the NC case can be calculated by

$$\gamma = \frac{\|\boldsymbol{p}^{NC} - \boldsymbol{p}^*\| - \|\boldsymbol{p}^{AI\text{-}C} - \boldsymbol{p}^*\|}{\|\boldsymbol{p}^{NC} - \boldsymbol{p}^*\|} \times 100\% \qquad (4)$$

where the variables $\boldsymbol{p}^*$, $\boldsymbol{p}^{NC}$, and $\boldsymbol{p}^{AI\text{-}C}$ represent the target point position, the focal point position in the NC case, and focal point position in the AI-C case, respectively. $\tilde{\boldsymbol{p}}^*$ and $\hat{\boldsymbol{p}}^*$, respectively, denote the target with max. and min. accuracy improvements. They can be obtained by

$$(\tilde{\boldsymbol{p}}^*, \hat{\boldsymbol{p}}^*) = \left(\underset{\boldsymbol{p}^*}{\operatorname{argmax}}\, \gamma, \underset{\boldsymbol{p}^*}{\operatorname{argmin}}\, \gamma \right) \qquad (5)$$

Phase spread metric (PSM) (Dillon et al. 2018) was used to evaluate the degree of phase aberration for each sample, which is defined as

$$PSM = 1 - \frac{\sum_{k=1}^{n} e^{j\varphi(n)}}{n}, \quad k = 1, 2, ... \qquad (6)$$

where e is Euler's number and j is the imaginary unit. A PSM value of zero indicates that all the elements are in phase, while a value of one indicates that the phases are distributed uniformly between 0 and 2π. To evaluate thermal ablation effectiveness, the thermal dose is usually calculated to quantify the thermal exposure at a particular target region. In general, cumulative equivalent minutes at 43°C (CEM_{43}) are introduced as a metric for thermal dose evaluation, which can be obtained by the following equation (Eranki et al. 2018):

$$CEM_{43}(t) = \int_{t_1}^{t_2} R^{(43 - T(t))} dt \qquad (7)$$

where t_1 and t_2 denote the starting and ending time of the HIFU process. $T(t)$ is the function of temperature over HIFU exposure time t. The constant R is 0.25 when $T(t)$ is smaller than 43°C and 0.5 otherwise.

4 | Results and Discussion

This section details phase aberration analysis, computational efficiency, focal targeting, and thermal ablation. The controller's tracking performance is tested by path-following tasks and also compared with a conventional model-based controller.

4.1 | Phase Aberration Analysis

To validate whether our correction policy is robust in phase modulation, we have to analyze the phase aberration effect using the MRI-based anatomy model. Validation was performed in (1) ground-truth (GT), (2) homogenous (HG), and (3) AI-C conditions. The GT phase patterns were collected using the time-reversal principle. In the HG case, the phases were directly calculated using geometry-based equations (Dillon et al. 2018), where only water media was applied to the anatomical model. Thirty samples in the liver ROI were randomly selected for validation. The correction performance was evaluated using two metrics related to beam focusing quality, that is, focal spot area (mm^2) and focal shift (mm).

First, we verified whether the collected phase pattern was reliable enough to be the ground truth for model training. The HG case acted as the baseline for comparison with the GT case, as no phase aberration exists when ultrasound propagates in HG water. For each sample, PSM (Dillon et al. 2018) was employed to represent the transducers' overall phase distribution, such that the overall phase difference between the two cases can be intuitively compared. As shown in Figure 5a, all the validation samples in the GT case exhibit significant PSM differences with the baseline, suggesting severe phase aberration caused by inherent tissue heterogeneity of our anatomical model. Given the phase pattern, in Figure 5b, the acoustic field was computed to obtain the focal shift result. The focal shifts of the samples in the HG case are within a relatively small value of 0.7 mm, most of which are close to 0 mm. This verifies that the simulation details, such as beam forward propagation, were correctly implemented. In addition, the GT case and the HG case lead to a mean focal shift of 0.4 mm and 0.24 mm, respectively, showing that the GT case is comparable with the baseline. A validation example was randomly selected for beam visualization (Figure 5c). Both beams are focused in an oval shape with similar focal shifts and focal areas. These similarities suggest that the data collection method in the GT case is suitable to be the gold standard to facilitate robust model training.

Then, we compared the focusing quality of the AI-C case with the GT case, so as to validate that our model is effective in aberration correction. We collected 649 GT samples for model training, and then phases of the 30 validation samples were computed using the pre-trained model. As shown in Figure 5d, high goodness of fit ($R^2 > 0.99$) implies that the PSMs of the two cases are significantly linearly related. The slope of the linear regression line is also near 1. All the samples are approximately located on the line, demonstrating our model's accurate phase modulation capability. The focusing results are shown in Figure 5e. For most samples, negligible focal area differences in the AI-C and GT cases can be observed. The mean focal area in the AI-C condition is 12.58 mm², which is near to that of the
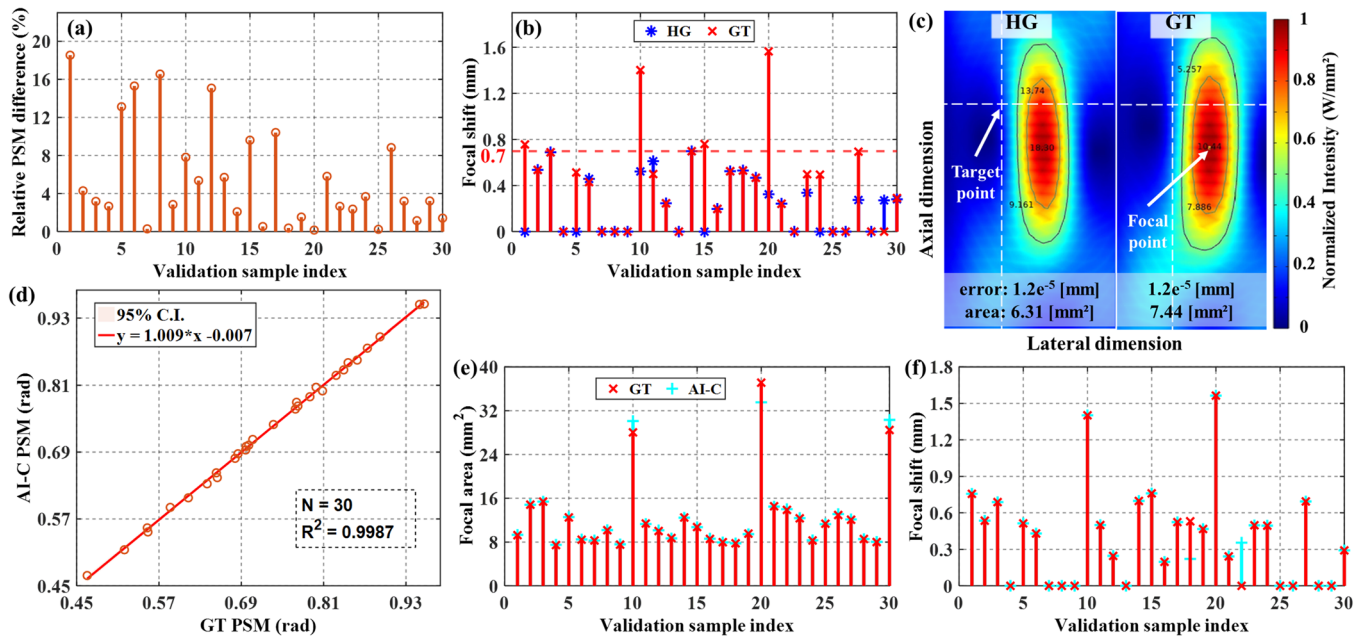
FIGURE 5 | Phase aberration analysis and modulation validation. (a) Relative phase spread metric (PSM) difference between homogenous (HG) and ground-truth (GT) cases calculated by $(PSM^{GT}–PSM^{HG})/PSM^{HG}$, where PSM^{GT} and PSM^{HG} represent the PSM values in the GT case and HG case, respectively. (b) Focal shift results in the HG and GT cases. (c) Focal spot visualization for a randomly selected validation sample. The focal spot with an intensity of –3 dB is delineated by a black solid line. The focal shift error is calculated by the distance between the focus point and the target point. (d) Linear regression results for the variable PSM in the AI-corrected (AI-C) and GT cases. (e) Focal area results in the AI-C and GT cases. (f) Focal shift results. [Color figure can be viewed at wileyonlinelibrary.com]

GT case (mean 12.56 mm²). A consistent finding is also obtained in focal shift, where the mean error of both cases is 0.40 mm. With these promising results, we could conclude that our model is robust in aberration correction, and the predicted phases enable effective beam focusing.

4.2 | Computational Efficiency

Since hundreds of lesion points need to be targeted in therapeutic applications, it would be essential to evaluate our models′ computational efficiency with regard to treatment efficacy, including our correction model and the motion mapping model. When a prescribed target/focal spot motion is fed into the pre-trained model, the computation time can be obtained by calculating the model processing time once the model predicts the phase signal command. Ten runs of the model computation time were recorded, and they were averaged for computational efficiency evaluation. One traditional full-wave simulation-based method, that is, the FDTD method, was included for comparison with our learning-based modulation model. Since the phase is determined by FE analysis (FEA) in this simulation method, the average time from 10 rounds of acoustic simulation was recorded. Note that phase correction is one of the most time-consuming steps in the whole treatment process (e.g., MRI scannings, anatomical segmentation), thus, only the phase modulation time was compared. All scripts were run on a standard server (AMD Ryzen Threadripper, 24 cores at 3.8 GHz with 64 GB RAM), without using any advanced parallel computing techniques accelerated by graphics processing units.

In general, more elements are generally expected for higher targeting or tracking accuracy, but it would lead to more computation resources. To balance the trade-off between transducer element number and computational cost, the models′ computational efficiency was evaluated with respect to (w.r.t) varying element number. As shown in Figure 6a, the traditional simulation method is computationally intensive, requiring approximately 15 min to complete phase computation for a single target. Such a long simulation time is currently prohibitive from a treatment standpoint. Empowered by ML, our model is much more computationally efficient with a mean of 3.621 ms, achieving a significant reduction in computational time without the need for FE modeling. This is 250 thousandths of the traditional method, indicating the potential to improve treatment efficiency in clinical practice. In previous works, Almquist et al. developed a full-wave phase aberration correction method for HIFU therapies, which requires approximately 15 min to compute phases (Almquist et al. 2016). Marsaca et al. employed an FDTD-based method for numerical simulations. The average computation time for a single simulation was 65 ± 3 h, requiring substantial computational resources (Marsac et al. 2017). The analytical method based on the geometric ray-tracing theory developed by Jin et al. (2020) could achieve a computation time of 402.1 ± 24.5 ms for each target point. However, our learning-based correction policy ensures much faster modulation compared with the previous models. Our ELM-based model consists of only one hidden-layer feedforward network, enabling initialization with random weights and rapid update of network parameters.

The computation time of our models w.r.t. element number is shown in Figure 6b. Obviously, more elements lead to an
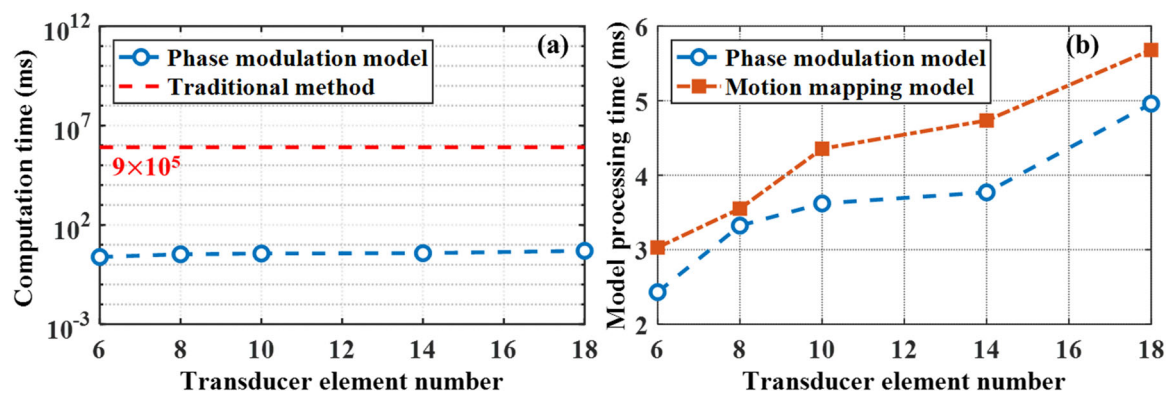
FIGURE 6 | Computational efficiency of two phase-aberration correction methods and a motion mapping model, with transducer element numbers ranging from 6 to 18. (a) Computation time comparison between our learning-based modulation model and the traditional method, which is presented on a logarithmic scale. (b) Processing time of our modulation model and motion mapping model resulting from transducer element number variation. [Color figure can be viewed at wileyonlinelibrary.com]

increasing computation time in both models. It is worth noting that an increment of elements from 6 to 18 even results in negligible additional time. The modulation model ensures rapid transduction within 4.96 ms. It would significantly reduce the correction time, demonstrating its potential to improve treatment efficiency in practice. Regarding our motion mapping model, we limit its computation time to 10 ms per time step, so as to maintain a high update frequency (> 100 Hz) for closed-loop control (K. Wang et al. 2021). Even with 18 elements, transduction would still take less than 10 ms (max. 5.68 ms), demonstrating the model's capability in real-time tracking.

4.3 | Phase-Only Targeting in Abdominal Organs

As point-by-point targeting accuracy is a crucial prerequisite for treatment efficacy in both LIFU and HIFU, we intended to investigate whether our correction policy enables accurate beam refocusing at the prescribed targets. When a hold-out testing sample's position was fed into the pre-trained phase modulation model, the phases would be computed for beam forming. Then, the targeting accuracy could be calculated with the distance between the focus point position and the target point. The NC case was also involved to show the aberration effect. To validate the mode's feasibility in widespread applications on abdomen organs, targeting was validated in two typical abdominal organs, that is, the liver and pancreas. The liver is demonstrated as the first example, in which constructive beam convergence would be challenging. As the largest solid organ, most likely, multiple or large tumors would need to be treated compared to other organs. Inevitably, numerous lesion points have to be targeted. Therefore, in Figure 7a, a broad ROI (12 mm × 20 mm) was defined, which is uniformly gridded with 77 hold-out testing samples, ranging from 65 mm to 85 mm depth.

The targeting accuracy results are depicted by bubble plots for intuitive comparison (Figure 7b). Before aberration correction, noticeable focal shifts with a mean of 0.828 mm can be observed in most samples. In contrast, our model with modulation ensures aberration compensation significantly with a mean error of only 0.317 mm. Although some targets are deep-seated

(e.g., 85 mm depth) with severe tissue heterogeneity, it still leads to a max. error of 0.937 mm, which satisfies typical clinical requirements for focal targeting (< 1 mm) (Tang et al. 2016). Some shallow targets without correction still receive clinically acceptable accuracy. The possible reason is that the weak tissue heterogeneity would induce limited aberration for those superficial targets. Box plots are employed to visualize the sample distribution in the liver ROI (Figure 7c), in terms of focal shift error and focal area. Such kinds of plots can offer a compact and informative representation of the samples. This also facilitates intuitive visualization and comparison of sample distribution across two groups. Additionally, a statistical test, that is, an independent sample t-test, was conducted for both focal error shift and focal area results, so as to determine whether a statistically significance difference exists between the NC and AI-C conditions. The I-values of the tests are shown in the box plots. Compared with the NC case, our model realizes an improvement of 50% in the liver, which corresponds to a low p-value (≤ 0.05). This indicates a statistically significant difference between the two cases, which is consistent with the result of the phase aberration analysis. Instead, the p-value of the focal area is 0.27, which suggests that no significant difference can be found between the NC and AI-C conditions.

The pancreas was used to further verify the targeting performance. The pancreas is a deep-located organ that requires beams to pass through many layers of tissues, resulting in severe phase aberration. The irregular tissue boundaries would induce further aberration. With these challenges in transabdominal focusing, the ROI (6 mm × 4 mm) located between the stomach and the liver's left lobe was selected (Figure 7a). Unlike the liver ROI, much fewer samples can be acquired in such a narrow ROI. One reason is that the samples with an ultrasound pathway covering the stomach have to be excluded, as the water–gas mixture in the stomach would destroy ultrasound transmission. We collected 57 training samples and 9 hold-out testing samples. Note that accurate targeting within the small region would be of particular clinical interest because such limited samples would bring challenges to model convergence. As shown in Table 1 regarding the pancreas, our model still results in a small mean error of 0.505 mm (smaller than one-third of the NC condition, mean of 1.662 mm), despite severe
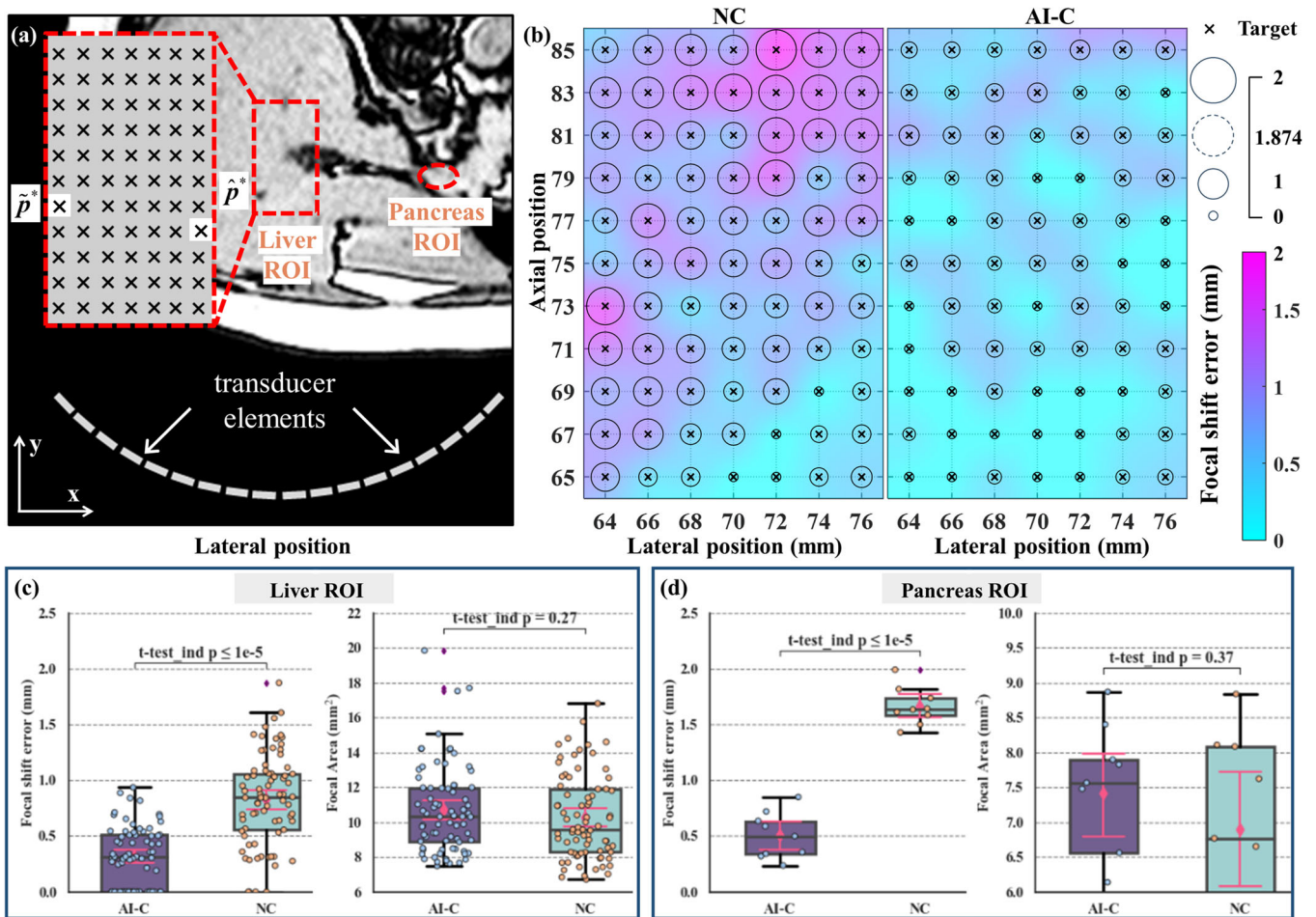
FIGURE 7 | Experimental results of point-by-point focal targeting in the liver and pancreas. (a) Seventy-seven sample points predefined in the liver region of interest (ROI) for targeted testing. Markers "×" in the liver ROI indicate the testing samples. The superscripts of p, "~" and "^", respectively, denote the sample with max. and min. targeting accuracy improvement. (b) Targeting results before (left half) and after phase-aberration correction (right half) in the liver. The accuracy of each sample is represented by a bubble. Statistical analysis results in the liver ROI (c) and pancreas ROI (d). In each box plot, the median values are displayed by the black horizontal lines. The upper and lower boundaries of the box represent the first and third quartiles, respectively. The minimum and maximum values, respectively, are indicated by the highest and lowest black horizontal lines. Outliers, which differ significantly from the rest of the data set, are displayed as individual points beyond the quartiles. [Color figure can be viewed at wileyonlinelibrary.com]

TABLE 1 | Statistical results of point targeting in the two organs.

Focal shift error (mm)	Liver			Pancreas		
	AI-C	NC	Improv.	AI-C	NC	Improv.
Mean error	0.317	0.828	61.71%	0.505	1.662	69.61%
Max. error	0.937	1.874	**50.00%**	0.851	1.991	**57.26%**

Note: Improv. denotes the improvement of AI-C over the NC case.

phase aberration. Similar to the liver, it is worth noting that our model attains a max. error of 0.851 mm in the pancreas, reaching clinical standard accuracy. Compared with the NC case, our model realizes an improvement of 57.26% in the pancreas. Such a substantial improvement indicates the potential of our method to be applied in a variety of solid abdominal organs. As shown in Figure 7d, a significant difference can be observed between the two cases ($p < 0.05$), while the t-test result for the focal area is nonsignificant ($p = 0.37$). This finding is consistent with the focal targeting results in the

liver ROI. These results also suggest that our model is not sensitive to tissue and acoustic parameters, implying the feasibility of our learning-based method in resolving full-wave phase aberrations. Moreover, our model was trained with 619 samples in the liver region, while the results in the pancreas are comparable with those in the liver. This implies that a training set containing only 57 samples is sufficient for accurate point targeting. It is worth noting that our learning-based approach could achieve full-wave modulation while ensuring rapid modulation, but previous model-based approaches suffer from

the trade-off between computational efficiency and correction accuracy. Moreover, our method enables accurate focal targeting (< 1 mm), while previous signal-based methods could not correct for focal location shift, as they can only access phase information from the predefined target point (Yeats and Hall 2023).

To visualize the acoustic intensity distribution, two representative examples in both organs are shown in Figure 8. The target with max. improvement (shaded in Figure 7a) in the liver is shown in Figure 8a. Attributing to accurate transduction, acoustic pressure can be effectively delivered to generate an oval-shaped focal spot, which is close to the target. Instead, the focus of the NC case shifts away from the target significantly (> 1.5 mm). In addition to tissue heterogeneity, some elements' sharp incident angles ($> 5°$) could be another factor, which may induce beam distortion (Bancel et al. 2021). Figure 8b shows the target with minimum focal shift differences (shaded in Figure 7a). The focal points in both cases have a small targeting error within 0.5 mm, owing to weak tissue heterogeneity. In the pancreas (Figure 8c), compared with the liver, waves have to pass through more tissue layers to arrive at the target. The physical effects (e.g., diffraction, refraction) would be non-negligible, inducing obvious targeting errors in the NC case. By imposing corrected phases, beam shape is restored with constructive beam-tissue interference, leading to max. accuracy improvement. In Figure 8d, despite marginal improvement, our model still regulates unwanted focal shift significantly to only 0.85 mm, maintaining a clinically acceptable accuracy. Note that training samples could be enriched, and model parameters (e.g., hidden nodes) could be further tuned to fulfill the accuracy requirement of specific applications, if necessary.

4.4 | HIFU Thermal Ablation

To explore point-by-point ablation performance in HIFU applications, we investigated whether thermal energy can be precisely localized without damaging normal tissues using our correction policy. The bioheat transfer module in the simulator was employed to simulate the thermal ablation procedure. The NC case was also involved for comparison. The liver is again chosen as the representative example, as liver tumor ablation could involve the most challenges, such as off-target heating and skin burn when ablating deep-seated targets.

First, we assessed the temperature rise induced by a few seconds of HIFU exposure. Two lesion points (i.e., targets)
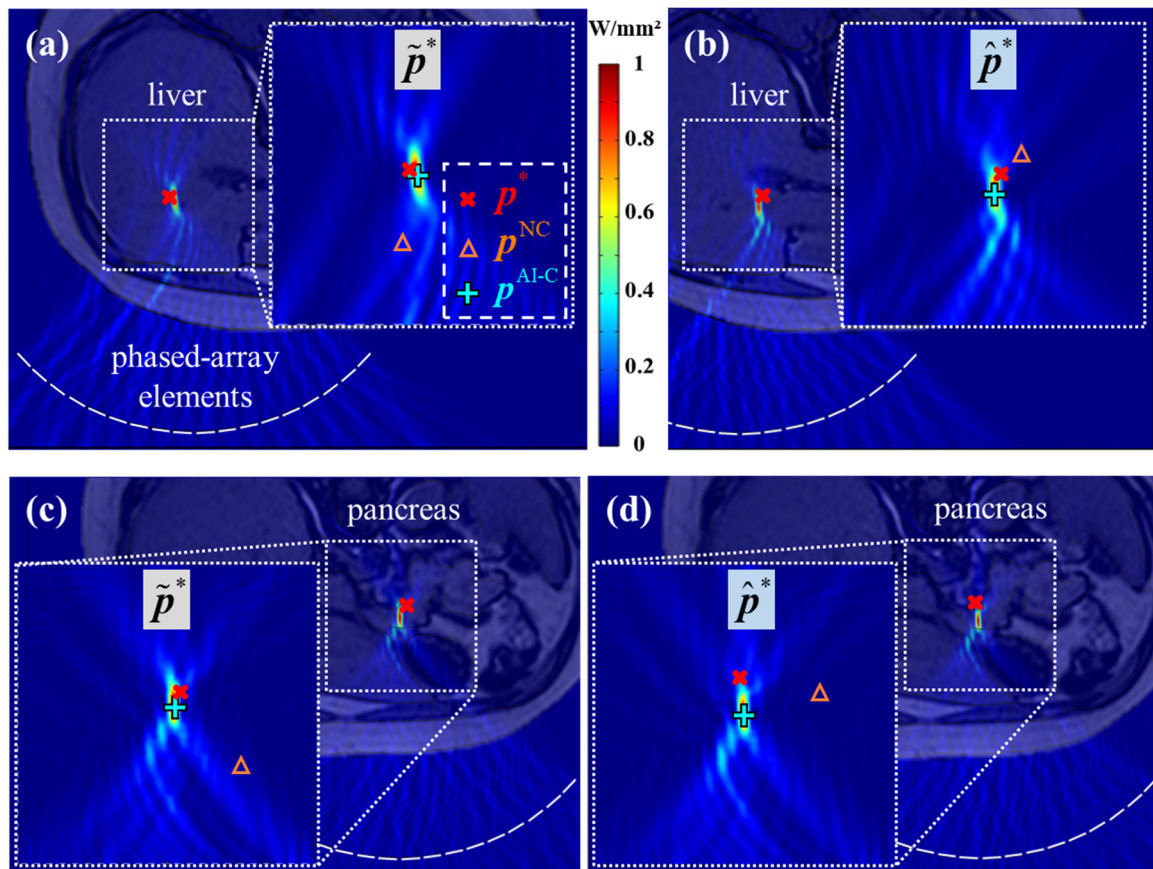

FIGURE 8 | Examples of focused ultrasound beams in the liver and the pancreas. Acoustic intensity maps were overlayed with the original magnetic resonance (MR) image for beam visualization. The beam pattern with max. (a) and min. (b) accuracy improvement in the liver region of interest (ROI). The superscripts of p, "*", "NC", and "AI-C", respectively, denote the target point, the focal point without phase-aberration correction, and the focal point with phase-aberration correction. The focused beam of the targets with the highest (c) and the lowest (d) error difference in the pancreas ROI. The focal shift error is decreased significantly after applying the AI-C phase for all the four targets. [Color figure can be viewed at wileyonlinelibrary.com]

were pinpointed in Figure 9a, where the deep target is 20 mm deeper than the shallow one. Figure 9b shows temperature variations at the two targets. Regarding the shallow target, after powering on for 1.3 s with corrected phases, the temperature rapidly elevates to the desired temperature of 60°C at 1.5 s. The same ablation time was applied in the NC case. Both cases reach 60°C in the same amount of time, while our model yields a 1.5°C greater rise than the NC case. Similarly, in terms of the deeper target located at 85 mm depth, the max. temperature was improved by 1°C in the AI-C case. These results indicate that the NC case ignoring phase aberration takes more time to reach the target temperature. It would substantially prolong the treatment time when ablating large or multiple tumors. Note that a tumor may be divided into thousands of lesion points to be ablated. Extended HIFU exposure would result in excessive heat accumulation, increasing the risk of skin burn. Instead, our accurate ML-enabled solution leads to rapid temperature rise and contributes to acoustic energy delivery to the target. Our approach can reduce the time necessary for thermal ablation, significantly improving heating efficiency.

To evaluate heating efficacy and safety, the thermal dose was measured for the two targets in Figure 9c,d. The thermal dose is highly associated with exposure time and temperature elevation and is distributed away from the target without correction for p_1^*. This suggests that the NC case could not effectively deliver ultrasound energy to the target, causing potential thermal damage to surrounding healthy tissues. In contrast, utilizing our model, the max. thermal dose across the heated ROI is significantly improved, which is highly localized around the target. Consistent results can be observed in the other target, that is, p_2^*. Although ultrasound waves have to travel through many layers of tissues for this deep target, leading to more energy loss, our solution still can offer sufficient thermal dose. These improvements demonstrate our model's advantage in improving heating efficacy.

Since safety is one of the major concerns in HIFU, the thermal maps at the peak temperature are shown in Figure 10 to intuitively assess heating safety. All the maps shared the same color scale. To ensure stable ultrasound transmission, degassed water acts as an acoustic coupling medium, such that the waves emitted by each element could penetrate the abdomen. For the target p_1^* (Figure 10a), in the NC case, obvious off-target heating can be observed, causing damage to the surrounding healthy tissues. After correction, a smaller, more intense, and more accurate HIFU spot is localized at the target, with negligible heating effects on normal tissues. Regarding the other target (Figure 10b), in the NC case, obvious overheating on the surrounding healthy tissues and superficial tissues (e.g., skin) can be observed. A much larger region may be damaged than that in p_1^*, which could be caused by severe aberration effects. After correction, the diffused HIFU spot before correction is intensified and sharpened. Negligible heat accumulation can be observed around the target. In addition, the associated reduction in near-field thermal accumulation would decrease the risk of skin burn and leave the surrounding areas unharmed, showing our model's effectiveness in thermal ablation.
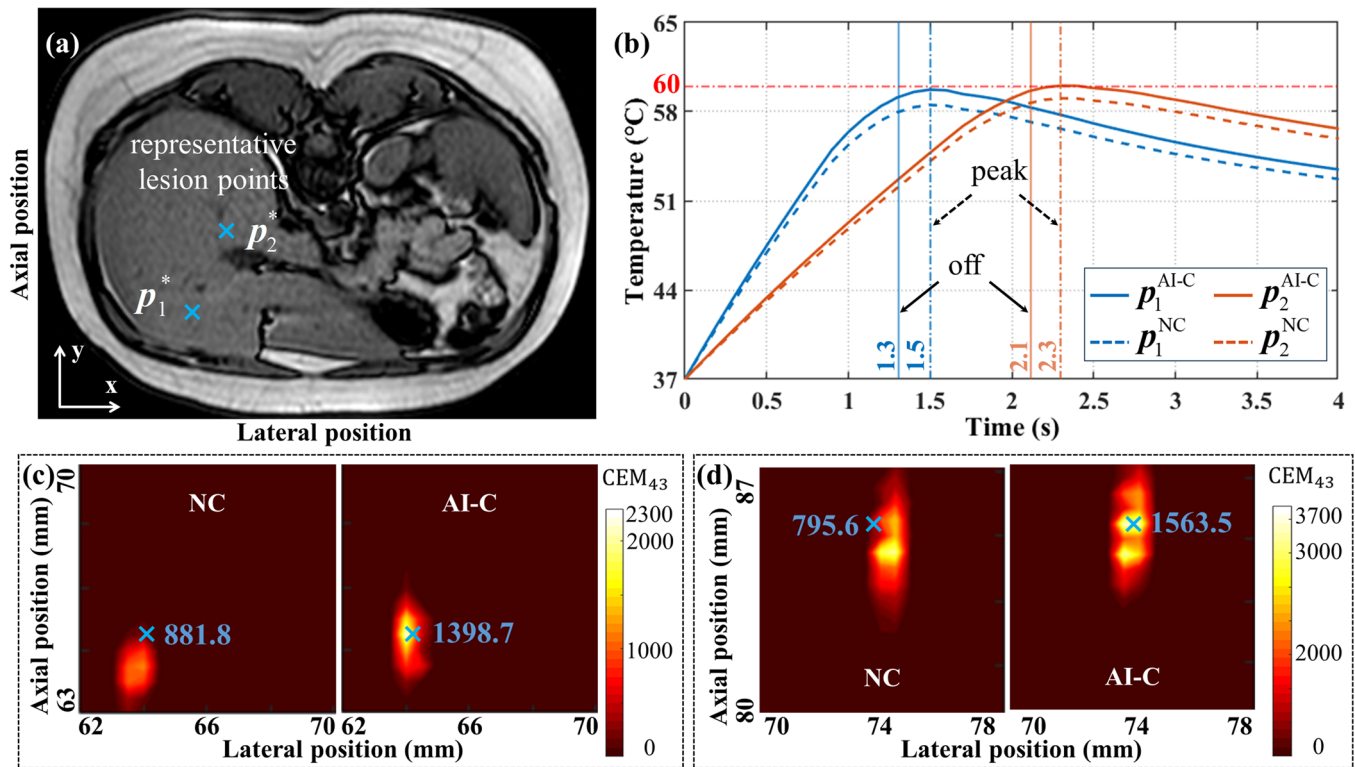

FIGURE 9 | High-intensity FUS (HIFU) ablation results. (a) Two representative lesion points for ablation testing. Markers "×" represent the pinpointed ablated lesions. The deep-located point (p_2) is 20 mm deeper than the shallow point (p_1). (b) Temperature versus time curves at the two targets in both non-corrected (NC) and AI-corrected (AI-C) cases. Ablation is performed with the same HIFU exposure time for each case. The thermal dose of the liver region of interest (ROI) for the shallow point (c) and the deep point (d). Labeled thermal doses are measured at the pinpointed lesion points. [Color figure can be viewed at wileyonlinelibrary.com]
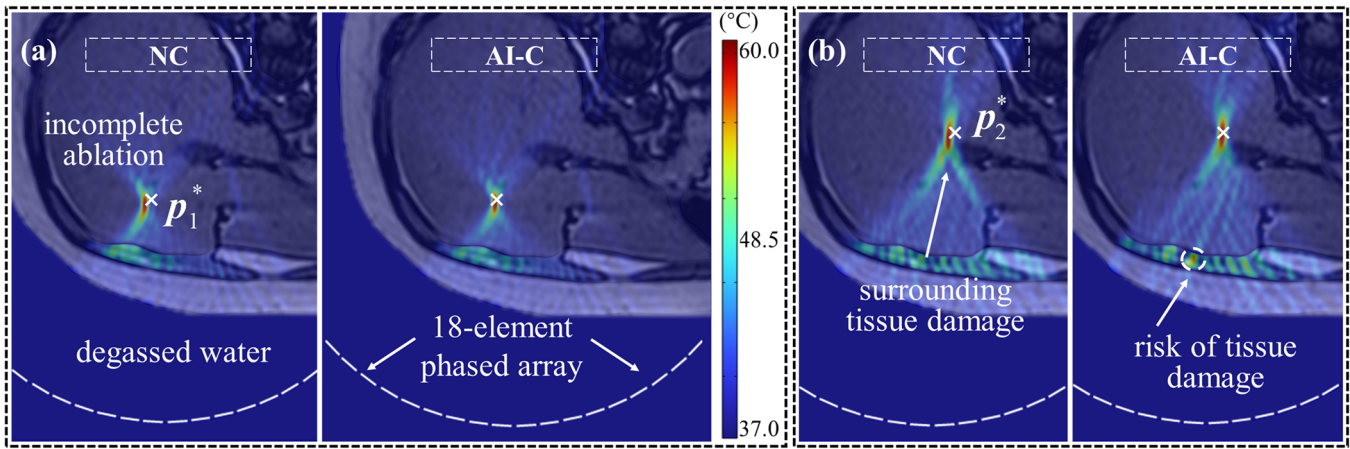
FIGURE 10 | Thermal maps (obtained at peak temperature) overlaid on the original magnetic resonance (MR) slices of the shallow point (a) and the deep point (b). After phase modulation (right half), the temperature can be increased and precisely localized at the targets, without overheating surrounding healthy tissues. Even for the deep target p_2, near-field intervening tissues remain unharmed. [Color figure can be viewed at wileyonlinelibrary.com]
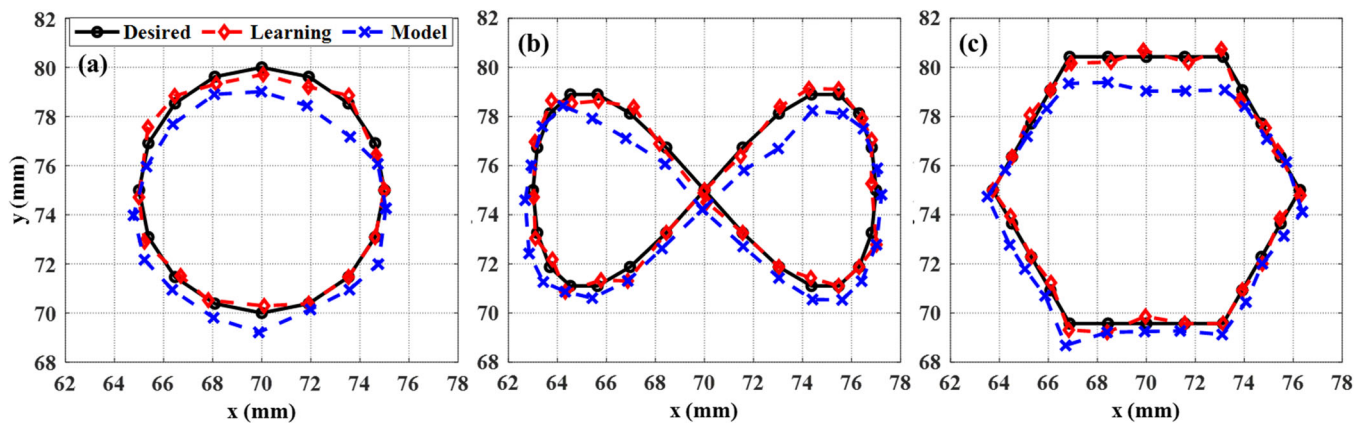

FIGURE 11 | Focal point steering with our closed-loop *learning*-based control and conventional open-loop *model*-based control. The focal spot is controlled to track the (a) circle, (b) infinity-shaped, and (c) hexagon trajectory. [Color figure can be viewed at wileyonlinelibrary.com]

4.5 | Learning-Based Closed-Loop Tracking Control

Accurate and real-time control of beam focusing and steering are essential for FUS treatments, especially considering that uniform heating distribution over a large target *region* is necessary for some applications (e.g., regional hyperthermia). Only with this type of control would it be possible to steer the focused spot to *continuously* and repeatedly track the predefined paths to cover a large ROI and allow for even temperature distribution. Here, our control policy incorporating the pre-trained

inverse mapping was tested with path-following tasks to evaluate its tracking performance. The simulator offers focus position feedback to close the control loop. Note that MRI (Chen et al. 2015) could also be a viable alternative to provide sensing feedback for closed-loop control in applications, e.g., MR-ARFI (Auboiroux et al. 2012). The conventional model-based method was involved for comparison, capable of providing a geometric solution (Dillon et al. 2018) for open-loop control. The tracking error is defined as the shortest distance between the spot position and the target point.

The target tracking performance for the three kinds of paths is shown in Figure 11, that is, circle, infinity-shaped, and hexagon trajectories. The model-based open-loop controller results in a mean error of 0.838 mm in Figure 11a, where an obvious deviation from the circle path can be observed. In the infinity-shaped path (Figure 11b) with varying curvature, the deviation diminishes slightly to a mean error of 0.688 mm. In particular, when following the hexagon trajectory in Figure 11c, it is notable that the focus point could follow the trajectory in the superficial region. However, the tracking error increases for the targets at the top of this path with a depth of around 80.2 mm or

Although our phase modulation solution is feasible to enhance HIFU safety, it is not capable of totally avoiding overheating, particularly for the deep target p_2^*. Some tissues are still overheated, indicating that phase correction is likely insufficient to solve the overheating problem completely. A possible reason is that the tissue damage may also originate from amplitude aberration, rather than only phase aberration, as equal power distribution was applied to the elements without considering amplitude-aberration correction.

in the sharp corners. This kind of error may result from severe tissue heterogeneity in the deep region. Regarding our learning-based controller, the focus point can be steered accurately along all three paths with a mean error smaller than 0.27 mm—whether on smooth paths (i.e., circle, infinity-shaped path) or on the hexagonal path composed of straight lines and sharp angles.

Detailed tracking results are summarized in Table 2. In all three paths, the max. errors of the model-based method are larger than the typical clinical requirement (< 1 mm). Such an FEA-based approach is computationally intensive and time-consuming. Its tracking accuracy is heavily dependent on accurate FE modeling and model parameter tuning. In contrast, incorporating position feedback allows our learning-based model to significantly enhance tracking performance. The maximum errors in all three paths meet clinically acceptable standards. In both smooth and sharp paths, our approach significantly improves tracking performance over the model-based method, achieving a 61.77%–70.39% reduction in mean error and a 52.20%–70.52% reduction in max. error. Note that the existing beam steering strategies still lack positional feedback, most of which use an open-loop approach. Although MR thermometry has been explored in previous works, they only offer thermal maps for HIFU applications. Focal spot position information could not be provided for the non-thermal LIFU process. In addition, our controller maintains a high tracking accuracy of < 1 mm when tracking the deep-seated targets in all the trajectories. This is typically challenging due to the need for rapid transduction while considering full-wave propagation inside highly heterogeneous tissues. Thus, it can be concluded that the learning-based controller is capable of accommodating nonlinear phase actuation for robust tracking, eliminating the need for model tuning. These results also demonstrate significant advantages of our controller in LIFU treatments over the traditional model-based method.

4.6 | Practical Implications

The presented correction and control approaches would be potentially beneficial to MRg-FUS transduction planning. The ML-based policies could offer efficient and accurate solutions to full-wave ultrasound modulation and control, without prior knowledge of heterogeneous media. Sub-millimeter focusing accuracy can be achieved, meeting clinical requirements for focal targeting (< 1 mm). It is anticipated that the modulation and control schemes partially address the concerns of precise and efficient ultrasound transduction. The advantages are expected to allow improved

accuracy and reduced treatment time for MRg-FUS procedures. Currently, our framework is primarily developed for MRg-FUS treatments of diseases in abdominopelvic organs, such as tumors in the liver. The successfully simulated validation tests in transabdominal FUS imply that our proposed learning-based concepts and techniques would facilitate transduction planning in other applications, for example, transcranial FUS.

Recently, the application of FUS has expanded from HIFU to non-thermal LIFU applications (O'Reilly 2024; Zamfirov et al. 2024), for example, neuromodulation (Legon 2021; Legon and Strohman 2024). Most previous works focus on HIFU treatments using MR thermometry feedback. However, MR thermometry guidance could only provide real-time thermal maps for HIFU, as there is no significant temperature rise during the LIFU process. This results in the demand for effective non-thermal imaging guidance to monitor focal spot generation, so as to enhance LIFU efficacy (Bancel et al. 2024). As a proof-of-concept, the current form of the framework has been validated in the simulated environment, which utilizes acoustic intensity maps to offer focal-spot position information. When extended to practical applications, it would be applicable to MRI environments, as advances in MRI technology (Cheung et al. 2020; Cheung et al. 2023; Dong et al. 2022) are readily available for ultrasound interference visualization. MR-ARFI can be an option, which can measure micrometric tissue displacement resulting from acoustic radiation force. This would allow monitoring of whether the ultrasound waves are focused accurately at a particular region. Additionally, it ensures fast image acquisition (e.g., ~1.05 s) (Auboiroux et al. 2012), which can be a reliable sensing feedback option in our framework. In practice, the temporal resolution of MR-ARFI feedback would depend on repetition time, matrix size, spatial resolution, field of view, and so forth. These factors can be balanced to accelerate data acquisition, thus ensuring fast feedback control of focal point motion. Once the focal point position is detected, our model-free controller could rapidly generate actuation signals (> 100 Hz) for the phased-array transducer, allowing simultaneous beam refocusing and steering.

Our proposed framework would also stimulate research on developing robot-assisted MRg-FUS systems (T. Li, Li, et al. 2024) by improving focal spot targeting. The robot platforms can act as ultrasound transducer positioners, offering sufficient focal-spot coverage of target organs. Additionally, the learning-based ultrasound modulation and control could be coordinated with robotic manipulation on the transducer, so as to ensure constructive ultrasound interference, for example, to reduce the risk of skin burns in HIFU treatments.

TABLE 2 | Mean and max. tracking error in three path-following tasks.

Error (mm)	Circle			Infinity-shaped			Hexagon		
	Learning	**Model**	**Improv.**	**Learning**	**Model**	**Improv.**	**Learning**	**Model**	**Improv.**
Mean	0.259	0.838	**69.09%**	0.263	0.688	**61.77%**	0.204	0.689	**70.39%**
Max.	0.653	1.366	**52.20%**	0.573	1.430	**59.93%**	0.411	1.394	**70.52%**

Note: Improv. denotes improvement of the learning-based controller over the model-based controller.

5 | Conclusion

This paper presents a novel learning-based framework for transabdominal MRg-FUS treatments. The framework integrates a phase-aberration correction model and a closed-loop model-free controller. In phase aberration analysis, the PSM of our correction model is significantly linearly related to the ground truth condition, showing the model's effectiveness in phase aberration compensation. Our full-wave correction policy can offer a rapid transduction solution within 5.0 ms. Compared with the conventional simulation-based method, it substantially reduces the correction time without the need for FE modeling (4.96 ms vs. 15 min), demonstrating its superior computational efficiency. Despite that the phase modulation model was trained with a relatively low number of training samples (i.e., 57), it could provide beam refocusing accuracy within 0.317 mm, even in the presence of severe tissue heterogeneity. Compared with the NC case, the model improves targeting accuracy (max. error) by 50% in the liver and 57.26% in the pancreas, meeting clinical standards for focal targeting (< 1 mm) in FUS treatments. Due to accurate phase correction, the ultrasound waves can converge precisely to thermally ablate the target point while preserving adjacent healthy tissues. Even for deep-seated targets, thermal damage to the surrounding tissue can be avoided without causing skin burns. This demonstrates the correction policy's potential to improve HIFU efficacy and safety.

Our model-free controller can approximate the global motion mapping of the phased-array system, enabling simultaneous focusing and steering for real-time position tracking. Image feedback is incorporated to detect the focal spot position and allow closed-loop tracking with nonlinear phase actuation in the path-following tests. Without having to tune the model parameters, our model-free control scheme could reduce mean tracking error by 61.77%–70.39%, as compared with the conventional model-based method. The beams could be focused while following the predefined trajectories, with a mean of 0.263 mm and a max. of 0.653 mm. The controller allowed tracking of a complex infinity-shaped pathway, with the ability to maintain control accuracy with a mean of 0.263 mm and max. 0.573 mm. The motion mapping model could facilitate fast control (< 5.7 ms) of a redundantly actuated phased-array system, thus allowing real-time beam motion control. The high update frequency (> 100 Hz) indicates its potential for future preclinical research and clinical applications. No previous study has investigated similar learning-based model-free strategies in MRg-FUS, making this the *first* to demonstrate model-free closed-loop control of a high-dimension phased-array ultrasound system.

Several limitations of our approach should be noted when applied to HIFU usage. The current phase-only correction policy may not be suitable for targets near blood vessels with high perfusion due to high energy dispersion. Compensation for amplitude aberration should be combined with the current correction policy to reduce the acoustic energy loss. In addition, when targeting critical nerve structures, amplitude modulation should be incorporated to alleviate focal obliquity and suppress grating lobes to improve treatment safety (Hughes et al. 2016). In our future work, the current proof-of-concept framework will be integrated with our previously developed MRI-guided robotic system (Dai et al. 2021). Integrating robotic transducer manipulation would provide more modulation solutions under the constraints of skin burn and beam focusing. Future

directions could also focus on the implementation of learning-based modulation and control schemes in real practice. A spherically curved 2D array will be employed so as to form the 3D-focused beam. Since each 1D array can be modulated to enable the individual beams to be in phase at a single target point, beam interference of all the 1D arrays would be constructive. MRI could provide focal spot position feedback for correction and control policies. Considering that the capabilities of MRI guidance have not been fully utilized (e.g., MR-ARFI), both acoustic interference and thermal feedback can be leveraged to accommodate modeling uncertainties and provide accurate intra-operative monitoring. This could ultimately ensure constructive beam interference for safe and accurate interventions. We also aim to perform further testing of our proof-of-concept framework in Ex Vivo and eventually In Vivo tissues.

Conflicts of Interest

The authors declare no conflicts of interest.

Data Availability Statement

The data that support the findings of this study are available from the corresponding author upon reasonable request. Qualified researchers with reasonable requests for access to the data should contact the corresponding authors. Any data use will be restricted to noncommercial research purposes.

References

Almquist, S., D. L. Parker, and D. A. Christensen. 2016. "Rapid Full-Wave Phase Aberration Correction Method for Transcranial High-Intensity Focused Ultrasound Therapies." *Journal of Therapeutic Ultrasound* 4, no. 1: 30.

Auboiroux, V., M. Viallon, J. Roland, et al. 2012. "ARFI-Prepared MRgHIFU in Liver: Simultaneous Mapping of ARFI-Displacement and Temperature Elevation, Using a Fast GRE-EPI Sequence." *Magnetic Resonance in Medicine* 68, no. 3: 932–946.

Bancel, T., B. Béranger, M. Daniel, et al. 2024. "Sustained Reduction of Essential Tremor With Low-Power Non-Thermal Transcranial Focused Ultrasound Stimulations in Humans." *Brain Stimulation* 17, no. 3: 636–647.

Bancel, T., A. Houdouin, P. Annic, et al. 2021. "Comparison Between Ray-Tracing and Full-Wave Simulation for Transcranial Ultrasound Focusing on a Clinical System Using the Transfer Matrix Formalism." *IEEE Transactions on Ultrasonics, Ferroelectrics, and Frequency Control* 68, no. 7: 2554–2565.

Chen, Y., W. Wang, E. J. Schmidt, et al. 2016. "Design and Fabrication of MR-Tracked Metallic Stylet for Gynecologic Brachytherapy." *IEEE/ASME Transactions on Mechatronics* 21, no. 2: 956–962.

Cheung, C. L., J. D. L. Ho, V. Vardhanabhuti, H. C. Chang, and K. W. Kwok. 2020. "Design and Fabrication of Wireless Multilayer Tracking Marker for Intraoperative MRI-Guided Interventions." *IEEE/ASME Transactions on Mechatronics* 25, no. 2: 1016–1025.

Cheung, C.-L., M. Wu, and G. Fang, et al. 2023. "Omnidirectional Monolithic Marker for Intraoperative MR-Based Positional Sensing in Closed MRI." *IEEE Transactions on Medical Imaging* 43, no. 1: 439–448.

CTS. 2024. Piezoceramics for HIFU Transducers. https://www.ctscorp.com/Resources/Blog/Piezoceramic-for-HIFU-Transducers.

Dai, J., Z. He, G. Fang, et al. 2021. "A Robotic Platform to Navigate MRI-Guided Focused Ultrasound System." *IEEE Robotics and Automation Letters* 6, no. 3: 5137–5144.

Dillon, C. R., A. Farrer, H. McLean, S. Almquist, D. Christensen, and A. Payne. 2018. "Experimental Assessment of Phase Aberration Correction for Breast MRgFUS Therapy." *International Journal of Hyperthermia* 34, no. 6: 731–743.

Dong, Z., X. Wang, G. Fang, et al. 2022. "Shape Tracking and Feedback Control of Cardiac Catheter Using MRI-Guided Robotic Platform—Validation With Pulmonary Vein Isolation Simulator in MRI." *IEEE Transactions on Robotics* 38, no. 5: 2781–2798.

Eranki, A., N. Farr, A. Partanen, et al. 2018. "Mechanical Fractionation of Tissues Using Microsecond-Long HIFU Pulses on a Clinical MR-HIFU System." *International Journal of Hyperthermia* 34, no. 8: 1213–1224.

Fang, G., M. C. K. Chow, J. D. L. Ho, et al. 2021. "Soft Robotic Manipulator for Intraoperative MRI-Guided Transoral Laser Microsurgery." *Science Robotics* 6, no. 57: eabg5575.

Fang, G., X. Wang, J. D. L. Ho, et al. 2022. "Epipolar Geometry-Based Visual Servoing of Soft Endoscopic Manipulator for Transoral Laser Ablation." *Advanced Intelligent Systems* 4: 2200197.

Gerhardson, T., J. R. Sukovich, A. S. Pandey, T. L. Hall, C. A. Cain, and Z. Xu. 2017. "Catheter Hydrophone Aberration Correction for Transcranial Histotripsy Treatment of Intracerebral Hemorrhage: Proof-of-Concept." *IEEE Transactions on Ultrasonics, Ferroelectrics, and Frequency Control* 64, no. 11: 1684–1697.

Guillemin, P. C., L. Gui, O. Lorton, et al. 2019. "Mild Hyperthermia by MR-Guided Focused Ultrasound in an Ex Vivo Model of Osteolytic Bone Tumour: Optimization of the Spatio-Temporal Control of the Delivered Temperature." *Journal of Translational Medicine* 17, no. 1: 350.

Hou, X., J. Jing, Y. Jiang, et al. 2024. "Nanobubble-Actuated Ultrasound Neuromodulation for Selectively Shaping Behavior in Mice." *Nature Communications* 15, no. 1: 2253.

Hou, X., Z. Qiu, Q. Xian, et al. 2021. "Precise Ultrasound Neuromodulation in a Deep Brain Region Using Nano Gas Vesicles as Actuators." *Advanced Science* 8, no. 21: 2101934.

Hughes, A., Y. Huang, A. Pulkkinen, M. M. L. Schwartz, A. M. Lozano, and K. Hynynen. 2016. "A Numerical Study on the Oblique Focus in MR-Guided Transcranial Focused Ultrasound." *Physics in Medicine and Biology* 61, no. 22: 8025–8043.

Hynynen, K. 2020. "Thermal Therapy Monitoring Using Elastography." In *Tissue Elasticity Imaging*, 135–155. Elsevier.

Hyvärinen, M., Y. Huang, E. David, and K. Hynynen. 2022. "Comparison of Computer Simulations and Clinical Treatment Results of Magnetic Resonance-Guided Focused Ultrasound Surgery (MRgFUS) of Uterine Fibroids." *Medical Physics* 49, no. 4: 2101–2119.

Jin, C., D. Moore, J. Snell, and D. G. Paeng. 2020. "An Open-Source Phase Correction Toolkit for Transcranial Focused Ultrasound." *BMC Biomedical Engineering* 2: 9.

Johnson, S. L., C. Dillon, H. Odéen, D. Parker, D. Christensen, and A. Payne. 2016. "Development and Validation of a MRgHIFU Non-Invasive Tissue Acoustic Property Estimation Technique." *International Journal of Hyperthermia* 32, no. 7: 723–734.

Kavur, A. E., N. S. Gezer, M. Barış, et al. 2021. "CHAOS Challenge-Combined (CT-MR) Healthy Abdominal Organ Segmentation." *Medical Image Analysis* 69: 101950.

Kaye, E. A., Y. Hertzberg, M. Marx, et al. 2012. "Application of Zernike Polynomials Towards Accelerated Adaptive Focusing of Transcranial High Intensity Focused Ultrasound." *Medical Physics* 39, no. 10: 6254–6263.

Kosnoff, J., K. Yu, C. Liu, and B. He. 2024. "Transcranial Focused Ultrasound to V5 Enhances Human Visual Motion Brain-Computer Interface by Modulating Feature-Based Attention." *Nature Communications* 15, no. 1: 4382.

Kwok, K. W., H. Wurdemann, A. Arezzo, A. Menciassi, and K. Althoefer. 2022. "Soft Robot-Assisted Minimally Invasive Surgery and Interventions: Advances and Outlook." *Proceedings of the IEEE* 110, no. 7: 871–892.

Kyriakou, A., E. Neufeld, B. Werner, M. M. Paulides, G. Szekely, and N. Kuster. 2014. "A Review of Numerical and Experimental Compensation Techniques for Skull-Induced Phase Aberrations in Transcranial Focused Ultrasound." *International Journal of Hyperthermia* 30, no. 1: 36–46.

Kyriakou, A., E. Neufeld, B. Werner, G. Székely, and N. Kuster. 2015. "Full-Wave Acoustic and Thermal Modeling of Transcranial Ultrasound Propagation and Investigation of Skull-Induced Aberration Correction Techniques: A Feasibility Study." *Journal of Therapeutic Ultrasound* 3, no. 1: 1–18.

Lee, K. H., D. K. C. Fu, M. C. W. Leong, et al. 2017. "Nonparametric Online Learning Control for Soft Continuum Robot: An Enabling Technique for Effective Endoscopic Navigation." *Soft Robotics* 4, no. 4: 324–337.

Legon, W. 2021. "Principles and Mechanisms of Focused Ultrasound Neuromodulation." *Brain Stimulation* 14, no. 6: 1747–1748.

Legon, W., and A. Strohman. 2024. "Low-Intensity Focused Ultrasound for Human Neuromodulation." *Nature Reviews Methods Primers* 4, no. 1: 91.

Li, F., J. Gallego, N. N. Tirko, et al. 2024. "Low-Intensity Pulsed Ultrasound Stimulation (LIPUS) Modulates Microglial Activation Following Intracortical Microelectrode Implantation." *Nature Communications* 15, no. 1: 5512.

Li, T., J. Li, L. Bo, et al. 2024. "Robot-Assisted Chirality-Tunable Acoustic Vortex Tweezers for Contactless, Multifunctional, 4-DOF Object Manipulation." *Science Advances* 10, no. 21: eadm7698.

Lipsman, N., Y. Meng, A. J. Bethune, et al. 2018. "Blood–Brain Barrier Opening in Alzheimer's Disease Using MR-Guided Focused Ultrasound." *Nature Communications* 9, no. 1: 2336.

Ljubic, A., T. Bozanovic, and Z. Vilendecic. 2009. "Sonographic Evaluation of Benign Pelvic Masses." *Donald School Journal of Ultrasound in Obstetrics and Gynecology* 3, no. 2: 58–68.

Luo, H., M. K. Sigona, T. J. Manuel, et al. 2022. "Reduced-Field of View Three-Dimensional MR Acoustic Radiation Force Imaging With a Low-Rank Reconstruction for Targeting Transcranial Focused Ultrasound." *Magnetic Resonance in Medicine* 88, no. 6: 2419–2431.

Macoskey, J. J., T. L. Hall, J. R. Sukovich, et al. 2018. "Soft-Tissue Aberration Correction for Histotripsy." *IEEE Transactions on Ultrasonics, Ferroelectrics, and Frequency Control* 65, no. 11: 2073–2085.

Marquet, F., M. Pernot, J. F. Aubry, et al. 2009. "Non-Invasive Transcranial Ultrasound Therapy Based on a 3D CT Scan: Protocol Validation and In Vitro Results." *Physics in Medicine and Biology* 54, no. 9: 2597–2613.

Marsac, L., D. Chauvet, and R. Greca, et al. 2017. "Ex Vivo Optimisation of a Heterogeneous Speed of Sound Model of the Human Skull for Non-Invasive Transcranial Focused Ultrasound at 1 MHz." *International Journal of Hyperthermia* 33, no. 6: 635–645.

Martin, D., R. Xu, and M. O'Reilly. 2024. "Simulation-Corrected Focusing to the Vertebral Canal." *Journal of the Acoustical Society of America* 155, no. 3_Suppl: A248.

McMahon, D., M. A. O'Reilly, and K. Hynynen. 2021. "Therapeutic Agent Delivery Across the Blood–Brain Barrier Using Focused Ultrasound." *Annual Review of Biomedical Engineering* 23, no. 1: 89–113.

Meng, Y., K. Hynynen, and N. Lipsman. 2021. "Applications of Focused Ultrasound in the Brain: From Thermoablation to Drug Delivery." *Nature Reviews Neurology* 17, no. 1: 7–22.

Meng, Y., C. B. Pople, D. Budiansky, et al. 2022. "Current State of Therapeutic Focused Ultrasound Applications in Neuro-Oncology." *Journal of Neuro-Oncology* 156: 49–59.

Mougenot, C., M. Tillander, J. Koskela, M. O. Köhler, C. Moonen, and M. Ries. 2012. "High Intensity Focused Ultrasound With Large Aperture Transducers: A MRI Based Focal Point Correction for Tissue Heterogeneity." *Medical Physics* 39, no. 4: 1936–1945.

Ng, Y. L., M. C. K. Lo, K. H. Lee, et al. 2021. "Development of an Open-Access and Explainable Machine Learning Prediction System to Assess the Mortality and Recurrence Risk Factors of Clostridioides Difficile Infection Patients." *Advanced Intelligent Systems* 3, no. 1: 2000188.

O'Reilly, M. A. 2024. "Exploiting the Mechanical Effects of Ultrasound for Noninvasive Therapy." *Science* 385, no. 6714: eadp7206.

Partanen, A., P. S. Yarmolenko, A. Viitala, et al. 2012. "Mild Hyperthermia With Magnetic Resonance-Guided High-Intensity Focused Ultrasound for Applications in Drug Delivery." *International Journal of Hyperthermia* 28, no. 4: 320–336.

Rosnitskiy, P. B., T. D. Khokhlova, G. R. Schade, O. A. Sapozhnikov, and V. A. Khokhlova. 2024. "Treatment Planning and Aberration Correction Algorithm for HIFU Ablation of Renal Tumors." *IEEE Transactions on Ultrasonics, Ferroelectrics, and Frequency Control* 71: 341–353.

Rouvière, O., A. Gelet, S. Crouzet, and J. Y. Chapelon. 2012. "Prostate Focused Ultrasound Focal Therapy—Imaging for the Future." *Nature Reviews Clinical Oncology* 9, no. 12: 721–727.

Santos, M. A., S. K. Wu, M. Regenold, C. Allen, D. E. Goertz, and K. Hynynen. 2020. "Novel Fractionated Ultrashort Thermal Exposures With MRI-Guided Focused Ultrasound for Treating Tumors With Thermosensitive Drugs." *Science Advances* 6, no. 36: eaba5684.

Schoen, S., and C. D. Arvanitis. 2020. "Heterogeneous Angular Spectrum Method for Trans-Skull Imaging and Focusing." *IEEE Transactions on Medical Imaging* 39, no. 5: 1605–1614.

Schoen, S., P. Dash, and C. D. Arvanitis. 2022. "Experimental Demonstration of Trans-Skull Volumetric Passive Acoustic Mapping With the Heterogeneous Angular Spectrum Approach." *IEEE Transactions on Ultrasonics, Ferroelectrics, and Frequency Control* 69, no. 2: 534–542.

Shen, L., Z. Tian, K. Yang, et al. 2024a. "Joint Subarray Acoustic Tweezers Enable Controllable Cell Translation, Rotation, and Deformation." *Nature Communications* 15, no. 1: 9059.

Shen, L., Z. Tian, K. Yang, et al. 2024b. "Acousto-Dielectric Tweezers Enable Independent Manipulation of Multiple Particles." *Science Advances* 10, no. 32: eado8992.

Siansonic. 2023. HIFU Transducers-High Intensity Focused Ultrasound. https://www.siansonic.com/products-ultrasonic-transducers-HIFU-transducers.

Su, H., K. W. Kwok, K. Cleary, et al. 2022. "State of the Art and Future Opportunities in MRI-Guided Robot-Assisted Surgery and Interventions." *Proceedings of the IEEE* 110, no. 7: 968–992.

Sun, T., Y. Zhang, C. Power, et al. 2017. "Closed-Loop Control of Targeted Ultrasound Drug Delivery Across the Blood–Brain/Tumor Barriers in a Rat Glioma Model." *Proceedings of the National Academy of Sciences* 114, no. 48: E10281–E10290.

Tang, T., T. Azuma, and K. Itani, et al. 2016. "A New Method for Absolute Accuracy Evaluation of a US-Guided HIFU System With Heterogeneous Phantom." Paper presented at the 2016 IEEE International Ultrasonic Symposium.

Vyas, U., E. Kaye, and K. B. Pauly. 2014. "Transcranial Phase Aberration Correction Using Beam Simulations and MR-ARFI." *Medical Physics* 41, no. 3: 032901.

Wang, J., S. Lu, S. H. Wang, and Y. D. Zhang. 2022. "A Review on Extreme Learning Machine." *Multimedia Tools and Applications* 81, no. 29: 41611–41660.

Wang, K., C. H. Mak, J. D. L. Ho, et al. 2021. "Large-Scale Surface Shape Sensing With Learning-Based Computational Mechanics." *Advanced Intelligent Systems* 3, no. 11: 2100089.

Wang, X., J. Dai, H. S. Tong, et al. 2023. "Learning-Based Visual-Strain Fusion for Eye-in-Hand Continuum Robot Pose Estimation and Control." *IEEE Transactions on Robotics* 39: 2448–2467.

Wong, F., L. Zhang, and Z. Wang. 2021. *Focused Ultrasound Surgery in Gynecology: Introduction and Application.* Springer.

Wu, Y., Z. Huang, Y. Liu, et al. 2024. "Ultrasound Control of Genomic Regulatory Toolboxes for Cancer Immunotherapy." *Nature Communications* 15, no. 1: 10444.

Yeats, E., and T. L. Hall. 2023. "Aberration Correction in Abdominal Histotripsy." *International Journal of Hyperthermia* 40, no. 1: 2266594.

Zamfirov, L., N.-M. Nguyen, M. E. Fernández-Sánchez, et al. 2024. "Acoustic-Pressure-Driven Ultrasonic Activation of the Mechanosensitive Receptor RET and of Cell Proliferation in Colonic Tissue." *Nature Biomedical Engineering* 9, no. 5: 742–753.

Zhou, B., B. Y. K. Leung, and L. Sun. 2017. "The Effects of Low-Intensity Ultrasound on Fat Reduction of Rat Model." *BioMed Research International* 2017, no. 2017: 1–8.